AIAA SciTech Forum
8-12 January 2024, Orlando, FL
AIAA SCITECH 2024 Forum

10.2514/6.2024-2041

Mass, Volume and Natural Frequency Scaling of Deployable Mesh Reflectors

Sahangi P. Dassanayake *, and Jong-Eun Suh †
California Institute of Technology, Pasadena, California, 91125, United States

Mark W. Thomson‡
Tendeg LLC, Louisville, Colorado, 80027, United States

Sergio Pellegrino§
California Institute of Technology, Pasadena, California, 91125, United States

This study presents a general design methodology for deployable mesh reflectors of any aperture diameter, focal length, and operational radio frequency. The reflectors consist of two triangulated cable nets attached to a deployable perimeter truss and prestressed against each other. Scaling laws are derived for the reflector mass, stowed volume, and fundamental natural frequency of vibration. A comprehensive design study is conducted considering the geometry, structural design of the reflector components, and optimization of the prestress distribution for mass efficiency. The launch envelope is identified as the limiting factor in the design of deployable reflectors, for building large reflectors in space. The natural frequency of the designed reflector is evaluated for a range of aperture sizes using a high-fidelity finite element model, and the natural frequency scaling law is established. This study proposes a semi-analytical model for the mesh reflector based on the homogenization of the structural components, which performs with good accuracy while ensuring significantly less computational effort.

I. Introduction

As space mission designs evolve with the advancement of technology, there is an increasing demand for high performance reflector antennas. Since the size of an antenna is critical to its performance, antennas with large apertures are desirable in achieving the required efficiency. On the other hand, there are requirements specifically for space-borne antennas in terms of higher mass efficiencies and higher packaging ratios, which are in contrast to the desired large apertures. Deployable mesh reflector antennas were introduced in the past few decades as a means of addressing this demand. Commercial systems are currently available from a number of suppliers, including Astro Aerospace Northrop Grumman, L3 Harris and Tendeg and are widely used for communication and scientific measurements. *Umbrella Reflectors* [1], where gores of metallic wire mesh are stretched across a series of parabolic ribs and *Wrap-Rib Reflectors* [2], where elastic thin shell ribs with a parabolic edge profile are wound around a central hub mechanism, are two initial concepts that were introduced for parabolic mesh reflectors. However, the achievable aperture sizes based on these initial design endeavors were limited to around 10 m, since achieving the required surface accuracy became increasingly difficult for larger apertures.

The *Tension Truss Concept* proposed by Miura and Miyazaki [3, 4] where a faceted reflective surface approximates to a paraboloid, with the triangular mesh facets pretensioned by normal forces applied to each joint introduced the possibility of overcoming the issue of scalability. Employing this approach, the *AstroMesh Reflector* – a novel concept was developed by Thomson and Hedgepeth [5, 6], where a pair of doubly curved cable nets are placed back-to-back in tension across the rim of a deployable perimeter truss. This concept has outperformed its predecessors in terms of surface accuracy and mass and volume efficiency, and has been successfully utilized for several space missions [7–9] in various aperture sizes ranging from 3 m to 25 m. Many variants of this original implementation by Hedgepeth and Thomson have been proposed [10, 11], AstroMesh becoming a fairly standard configuration for deployable mesh reflectors.

*Graduate Student, Graduate Aerospace Laboratories, AIAA Student Member.
†Postdoctoral Researcher, Graduate Aerospace Laboratories, AIAA Member.
‡Chief Technology Officer
§Joyce and Kent Kresa Professor of Aerospace and Civil Engineering, Graduate Aerospace Laboratories, AIAA Fellow.

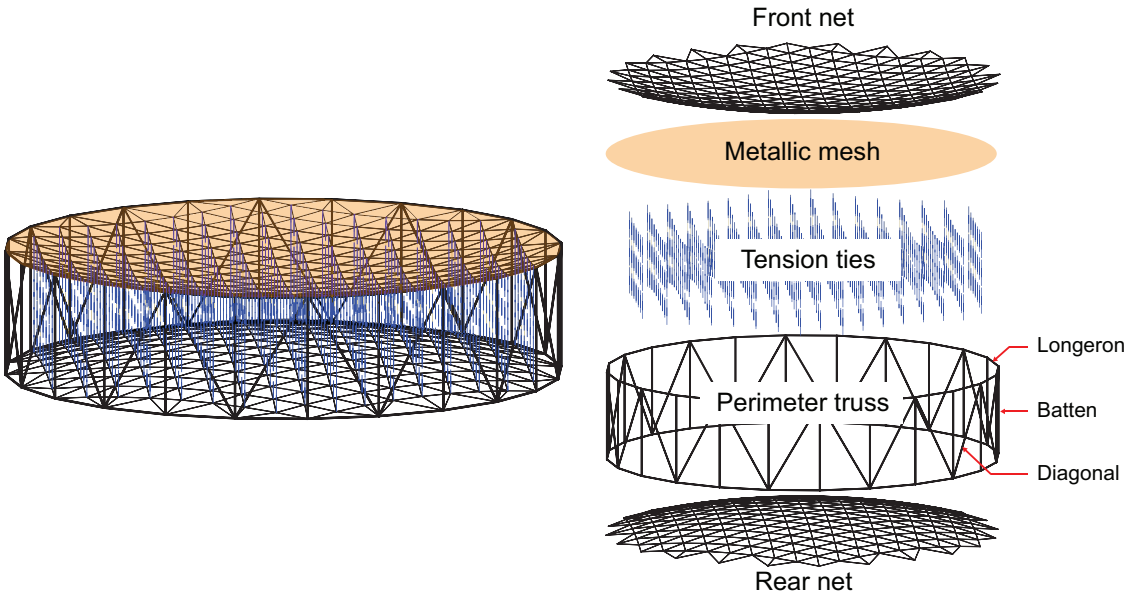

Fig. 1 Structural architecture of a faceted deployable mesh reflector, based on [5, 6]

Figure 1 shows the structural architecture of this reflector, which could be classified into three major components: the two cable nets, the metallic wire mesh, and the deployable perimeter truss [6]. The front and rear cable nets approximate identical paraboloids, supported by the perimeter truss and tensioned by ties stretched across corresponding node pairs on the two nets. The radio frequency (RF) reflective metallic mesh is attached to the underside of the front net, designed for operating the antenna at a specified radio frequency. The deployable perimeter truss consists of identical articulated parallelogram repeating units formed by two longerons (i.e., struts placed in the horizontal plane and forming the 'rim' of the truss in Fig. 1), two battens (i.e., struts placed in a vertical plane in Fig 1), and one diagonal that laterally braces the parallelogram and is allowed to extend to stow the truss into a hollow barrel-like shape. The cable nets and metallic mesh rest inside this structure during stowage. High stiffness and dimensional stability of the structure under thermal cycles during operation of the deployed and prestressed structure is ensured by selection of high-modulus and thermally stable material for the structural members.

The accuracy of the approximation by triangular facets (formed by cable elements as shown in Fig. 1) on the reflective surface is determined by facet size, which is related to the cable element lengths, and hence the cable net node density on the paraboloid. The facet size is dependent on the operational RF of the reflector, and is determined to provide the required approximation measured by the surface RMS error, δ_{rms}. As evident from numerous form-finding studies, geometric imperfections and high prestress variations along the cable net adversely affect the surface accuracy and stability of the surface, and hence the mesh reflector gain [12–15]. The dynamic response of the reflector has a significant impact on the design, since even small deformations caused by dynamic disturbances would degrade the antenna performance. Avoiding coupling with the attitude control system of the spacecraft [16–19] is key to improving dynamic performance of the reflector.

The feasibility of the deployable mesh reflector concept for specific missions is evaluated by the basic metrics of its mass and stowed volume (which determines launch selection), and the natural frequency of vibration (which determines its dynamic response during operation), whose effects become more critical for larger apertures. Previous studies have focused on improving reflector gain and RF efficiency via surface accuracy, with no reports on the mass and volume efficiencies of the proposed designs despite their significance for the design. With the exception of the trend of mass increase against the size of the reflector for diameters up to 25 m, in Thomson [6], no systematic study has been published based on these metrics. Moreover, most published numerical and experimental studies investigating the dynamic behavior of the mesh reflectors require high-fidelity numerical models and experimental models [17, 19], an inefficient approach for studies across a large range of scales and specially for analyzing extremely large structures with numerous structural elements.

The basis of the presented scaling study is a general design methodology for faceted mesh reflector antennas. Starting from a simple approximation of the geometric error associated with faceting the paraboloid geometry, the maximum acceptable size of the facets is estimated. Then, for this basic design, the required connectivity between the edges of the faceted surface and the deployable perimeter truss is investigated, to ensure that the front cable net has a unique prestress distribution (i.e., to form a statically determinate structure) and has a unique shape (i.e., it is a kinematically determinate structure). Different cable net configurations are explored accordingly to achieve the desired reflective surface shape. Following the determination of structure geometry, an optimization algorithm is proposed to obtain a more uniform, and hence stable level of prestress distribution in the cable net by varying the forces in the tension ties. What follows herein is a comprehensive design study for sizing the structural components of the prestressed mesh reflector to achieve appropriate margins against all relevant failure modes.

Deployable mesh reflectors for an operational RF of 10 GHz and aperture diameters up to 200 m are designed using this methodology. Scaling laws are determined for the mass, stowed volume, and natural frequency of vibration of the reflector. The launch envelope limits for deployable mesh reflector designs in space is investigated by considering current launch vehicles. This study also proposes a scalable semi-analytical model for the mesh reflector, capable of providing insights into the dynamic response of large reflectors while significantly reducing the computational effort as opposed to the numerical analysis of high-fidelity models. This paper is organized as follows. We start by describing the reflector geometric design and optimization of the prestress distribution in the structure, followed by the structural design. Then we propose the scaling laws for the mass and the stowed volume. The scaling of the natural frequency is then derived, and finally a semi-analytical model for estimating the fundamental natural frequency is proposed.

II. Geometry, Prestress Optimization and Structural Design of Mesh Reflector

A. Geometry, and design for kinematic and static determinacy

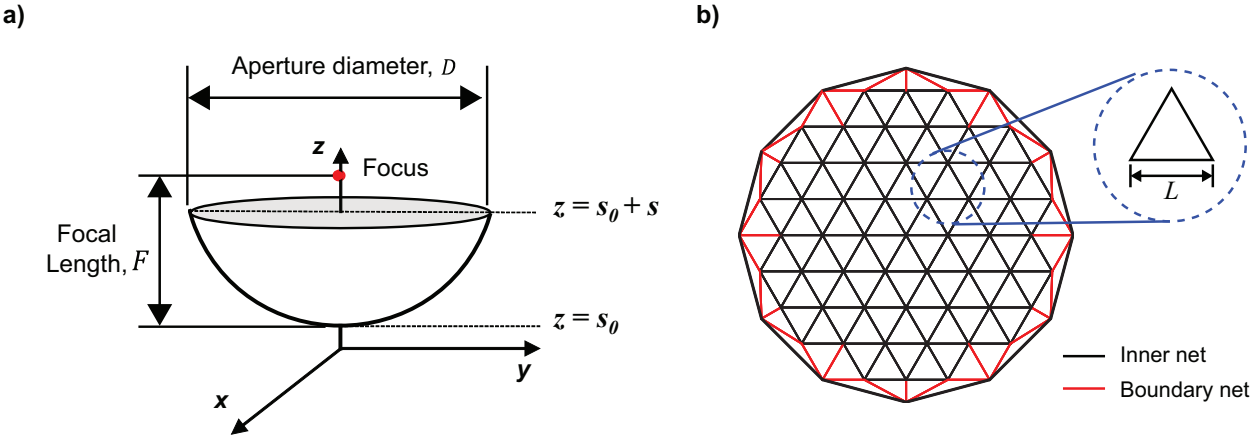

Fig. 2 a) Geometry of a paraboloidal reflector, and b) cable net configuration

Since parabolic surfaces maximize the antenna directivity [20, 21], this design assumes a paraboloid reflective surface. A circular paraboloid surface with axis z, focal length, F, and z-offset s_0 is shown in Fig.2a. The general equation for the paraboloid surface is presented in Eq. (1), and the closest distance between two cable nets (i.e., $2s_0$) is set to be a constant value (= 0.1 m) for all the reflector designs considered in this study.

$$s_0 + \frac{(x^2 + y^2)}{4F} = z \tag{1}$$

Geometric parameters of interest for a parabolic reflector are its operational frequency f and F/D ratio, where D refers to the aperture diameter. Higher F/D values indicate shallower reflectors, and for all designs, this ratio is set to be 1.0. Approximating a given axisymmetric paraboloid by a spherical cap of radius R, leads to the following relationship [22]:

$$R = 2F + \frac{D^2}{32F} \tag{2}$$

The paraboloid surface is approximated by equilateral triangular facets of size L, forming a hexagonal tessellation as shown in Fig. 2b. Faceting of the smooth paraboloid surface leads to a systematic surface error. The root-mean-square (RMS) value of this geometric error, is expressed as [23]:

$$\delta_{facet} = \frac{L^2}{8\sqrt{15}R} \tag{3}$$

Neglecting other error sources such as thermal distortions, spillover, aperture taper, cross polarization etc. and assuming that the geometric faceting error is the only source of surface RMS error (i.e., $\delta_{RMS} = \delta_{facet}$); the required surface RMS error for a reflector operating at 10 GHz is set to be 0.6 mm by the operational wavelength (= $\lambda/50$). Then, the maximum allowable facet size is obtained from Eqs. (2) and (3). The maximum allowable facet size is found to increase proportionally to $\sqrt{D}$ as the diameter of the reflector increases.

Figure 2b presents the cable net configuration of the mesh reflector. Once L is determined for a reflector of given D and F/D, the number of subdivisions, $n = 0.5D/L$ is calculated to derive the tessellation. The elements forming the cable net can be classified to two sections: *inner net* or the cables forming the hexagonal tessellation of equilateral triangles (black solid lines in Fig. 2b) and the *boundary net* or the cables connecting the inner net to the perimeter truss (red solid lines in Fig. 2b). The nodes in the inner net are defined as *free nodes*, and are connected by tension ties between the front and rear nets. Although the geometry of the inner nets is unique for a given facet size, the boundary net configuration varies depending on the number of bays in perimeter truss and the nature of their connections to the inner nets. It is assumed that each node in the perimeter truss supports the same number of free nodes, n_c. The number of subdivisions in the perimeter truss is defined as n_t. Analyzing the member forces of perimeter truss and cable net requires consideration of the boundary conditions applied to the structure, chosen such that a statically and kinematically determinate structure is obtained. This was investigated using the extended Maxwell's equation and the rank of the equilibrium matrix [24, 25], focusing on attaining the desired unique shape of the surface and a unique equilibrium solution for the prestressed structure. This analysis leads to the conclusion that these properties of the reflector depend upon the net geometry; only the configurations consisting of triangular facets without cross wires are found to be both kinematically and statically determinate, and can be described as follows:

$$n - 2 = (n_t - 1)\,(n_c - 1) \tag{4}$$

For this study, the perimeter truss has been designed to have half the density of the net accordingly. Therefore, each batten supports three free nodes with boundary cables (i.e., $n_c = 3$ in Eq. (4)). The lengths of the longerons, battens, and diagonals were determined based on the cable net geometry.

B. Prestress optimization

The front and rear cable nets are prestressed by the tension ties. Since the structure has been designed to be statically determinate, for any given geometry of the two nets, the prestress distribution ($\underline{P}$) of the cable nets is uniquely determined by equilibrium equations written for each free node i of the nets connected to N nodes, once the tension tie forces are chosen. An example is as follows;

$$\sum_{j}^{N} \left[\frac{x_i - x_j}{L_{ij}}\right] p_{ij} = t_{i,x} \tag{5}$$

where, L_{ij}: length of cable element $ij = \sqrt{(x_i - x_j)^2 + (y_i - y_j)^2 + (z_i - z_j)^2}$
p_{ij}: tension force in cable element ij
$t_{i,x}$: tension tie force applied to node i in the global x direction

The simplest approach of applying a single tension tie force to all free nodes resulted in cable elements near the transition region between the inner and boundary nets undergoing compression. Increasing the tension tie force applied at the free nodes in this region by a factor α (determined by a trial-and-error process) was found to eliminate this compressive prestress (see Fig. 3b), and also resulted in lower overall mass of the structure. Hence, the possibility of reducing the structural mass by way of a more uniform prestress distribution due to more than two distinct tension tie forces was formally explored, by formulating an optimization problem. While a distinct tension tie force can be applied at each free node theoretically, for simplicity of practical implementation and utilizing the six-fold rotational symmetry

of the hexagonal tessellation, the number of distinct tension tie forces applied was set equal to the number of *rings* (n_r) the tessellation can be divided into, i.e. $n + 1$ (see Fig. 3a).

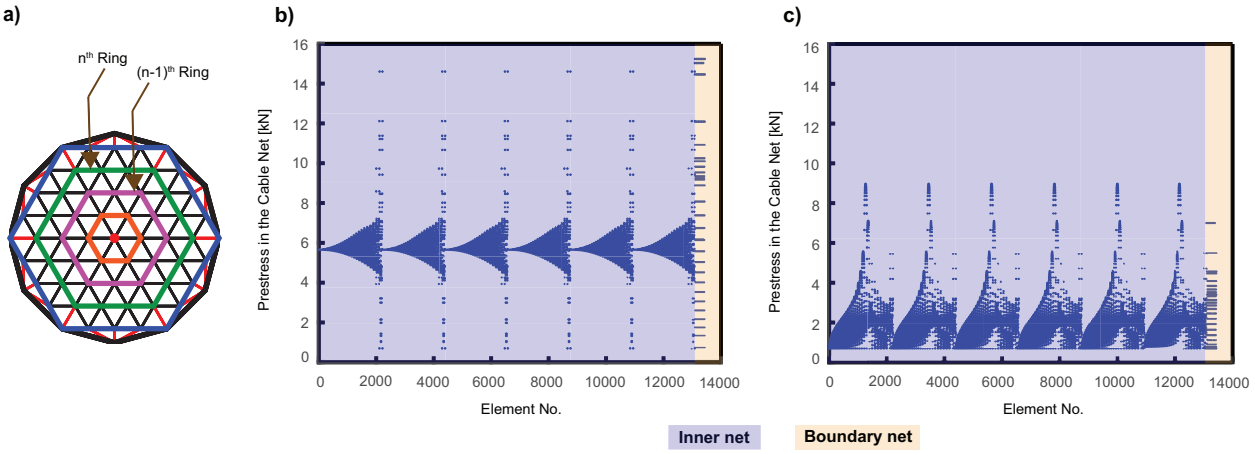

Fig. 3 (a) Definition of *rings* in inner net, Comparison of cable prestress distributions for $D = 200$ m, $F/D = 1.0$ corresponding to (b) 2 distinct tension tie forces ($\alpha = 1.7$), and (c) $(n + 1)$ no. of distinct tension tie forces

A set of independent and representative tension tie force distributions T were prescribed such that the k^{th} distribution (T^k) would consist of unit tension at all of the free nodes on k^{th} ring, and zero tension at all other free nodes. The prestress distribution in equilibrium with T^k is given by P^k. Collecting these variables into two vectors, gives:

$$T = \left[\underline{T}^1 \ \underline{T}^2 \ \dots \ \underline{T}^k \ \dots \ \underline{T}^{n_r}\right] \tag{6a}$$

$$P = \left[\underline{P}^1 \ \underline{P}^2 \ \dots \ \underline{P}^k \ \dots \ \underline{P}^{n_r}\right] \tag{6b}$$

The optimization algorithm was defined such that for a general tie force distribution $T\alpha$ and the corresponding cable tensions $P\alpha$, the coefficients α_k are constrained to be positive to ensure that all tension tie forces are positive. To ensure sufficient level of pretension in the cables to keep them both under tension and sufficiently straight when they are loaded by the prestressed metallic mesh, the minimum required tension $(P_{ij})_{min}$ applied to the cable elements is constrained as follows [26]:

$$(P_{ij})_{min} = 10\sigma L_{max} \tag{7}$$

where, σ: biaxial prestress in the metallic mesh
L_{max}: maximum cable length in the net

Different indicators of the prestress distribution were considered for the objective function to be minimized, and the corresponding maximum compressive forces in the perimeter truss and range of cable tensions ($\frac{(P_{ij})_{max}}{(P_{ij})_{min}}$) in the net were evaluated as the two metrics. Their direct contribution to the overall structural mass is described in Sections II.C and III. This analysis showed that applying more than two distinct tension tie forces leads to improvements in both metrics of interest; minimizing the average batten force in the perimeter truss led to $\sim$ 30% reduction in mass, with $\sim$ 40% reduction in the range of cable tensions and was selected as the objective function to be minimized accordingly.

Once the optimizing linear coefficients $\alpha_{k,opt}$ are determined, the optimum tension tie force distribution and corresponding cable forces can be calculated as follows;

$$T^{opt} = \left[\sum_{k=1}^{n_r} a_{k,opt} T^k\right] \tag{8a}$$

$$P_{opt} = \left[\sum_{k=1}^{n_r} a_{k,opt} P^k\right] \tag{8b}$$

Figure 3c provides a graphical representation of the optimized prestress distribution in the cable net for D = 200 m, F/D = 1.0, σ = 5.0 N/m, and it is interesting to compare this with Fig. 3b and observe that the majority of cable tensions are significantly lower in the optimized case.

C. Structural design

Knitted gold-plated molybdenum wire mesh with an areal density (ρ_{mesh}) of 0.025 kg/m^2 was selected for the reflector design. The required level of the biaxial prestress by the mesh to prevent ohmic losses during operation, σ, was set to be 5 N/m. Thin CFRP strips form the cables in the front and rear nets; the CFRP material being M55J carbon fiber (E_{1f} = 540 GPa, ρ_f = 1910 kg/m^3) in a thermoplastic matrix (E_m = 3.5 GPa, ρ_m = 1600 kg/m^3) [27]. The fiber volume fraction was assumed to be 0.6, and the longitudinal modulus, E_{CFRP}, and density, ρ_{CFRP}, of CFRP were calculated accordingly via the rule of mixtures (E_{CFRP} = 325.4 GPa, ρ_{CFRP} = 1786 kg/m^3). The cross-section of the CFRP strip was chosen to be rectangular, the width and thickness being 6 mm and 150 μm respectively. Same cross-section was assumed for reflectors of all apertures.

The optimization process described in Section II.B was utilized to determine the pretension of the nets, and equilibrium equations of the truss joints were evaluated to determine the compression forces in the perimeter truss. The perimeter truss (i.e., longerons, battens, and diagonals) is subjected to relatively high compression due to the applied pre-tension. A circular tube cross section was assumed for all members, with the minimum diameter set to be 5 mm to avoid impractical designs. The size of the longeron was determined first, considering that it is the member subjected to the largest compression. Their thickness was set to 1 mm for all apertures; only the longeron radius was considered a design variable, determined against the global critical buckling failure criterion assuming pin-ended conditions, with a safety factor of 2. Battens were designed to have the same diameter as the longerons, with the minimum thickness set at 1.25 mm, and the actual thickness determined based on the same buckling criterion and the subjected level of compression in the battens. In the equilibrium state, theoretically the diagonals are not subjected to any compression, although they are loaded in bending during deployment; thus, the size of the diagonals was simply set to be the same as the longerons, but with a thickness of 0.75 mm. Choosing all members to have the same diameter enables simpler and lighter joint design. The radius and thickness of the longeron, batten, and diagonals for the reflector designs of D = 10 m, 100 m, 200 m are presented in Table 1.

Table 1 Size of perimeter truss members, for F/D = 1.0

D(m)	Radius of Longeron/ Batten/Diagonal (mm)	Thickness of Longeron (mm)	Thickness of Batten (mm)	Thickness of Diagonal (mm)
10	6.145	1.00	1.25	0.75
100	45.434	1.00	1.25	0.75
200	94.102	1.00	1.25	0.75

Joints contribute to $\sim$ 15% of the overall mass of the structure. A scalable parametric design process based purely on the geometry (longeron diameter and thickness for each aperture) was followed in determining the joint mass, with the same CFRP material as the truss members.

III. Scaling of Mass and Stowed Volume

A. Estimating mass and stowed volume

As described in Section I, an AstroMesh-type deployable mesh reflector allows the folding of the perimeter truss into a cylindrical configuration with a smaller diameter. The structural mass and stowed volume constrain the possibility of launch of a deployable structure with a specific aperture; thus, the mass, stowed diameter, and stowed height of the mesh reflector are investigated for the complete aperture range of interest.

The total mass of the reflector was estimated to be the sum of contributions from the different components; cable net elements (m_n), metallic mesh (m_{mesh}), perimeter truss (m_{truss}), tension ties (m_{tt}), joints (m_j), and deployment actuators (m_{dep}):

$$m_{total} = m_n + m_{mesh} + m_{truss} + m_{tt} + m_j + m_{dep} \tag{9}$$

The mass of the cable nets, m_n, is calculated as:

$$m_n = \rho_n A_n \sum L_{ij} \tag{10}$$

where, ρ_n, A_n, and L_{ij} refer to the material density, cross-sectional area of strip, and length of strip ij, respectively. It is assumed that the metallic mesh covers the complete paraboloid surface of the front net, and hence m_{mesh} is obtained by multiplying the areal density of the mesh, ρ_{mesh} with A_{mesh}, where A_{mesh} is the area of the paraboloid surface. The mass of the perimeter truss m_{truss} and the mass of joints m_j are calculated based on the structural design described in Section II. The mass of the tension ties and seams in the mesh, m_{tt}, is assumed to be twice m_{mesh}, and the mass of deployment actuators m_{dep} is assumed to be 10% of the total mass of the reflector.

Since the structure folds into a cylinder of a smaller diameter, the perimeter of the stowed configuration (P_{stowed}) is mainly limited by the contact between adjacent joints, and the height of the stowed configuration (H_{stowed}) is related to the length of the truss members. The diameter of the stowed configuration is estimated from the perimeter of the stowed cylinder, as $D_{stowed} = P_{stowed}/\pi$.

Figure 4 indicates the variation of the equivalent areal density of the reflector components versus the aperture, for $F/D = 1.0$. As shown in Fig. 4a, the areal density generally increases proportional to the diameter of the reflector for the non-optimal design, the main reason being the rapid increase of m_{truss}. In contrast, the compressive forces applied to the perimeter truss are much smaller in the optimal design, leading to an approximately constant areal density over the range of apertures as seen in Fig. 4b. While this difference between the two approaches is fairly small for apertures below 50 m, it becomes quite significant for larger apertures. The lower prestress of the truss reduces the size of its members and achieves almost a factor of two reduction in areal density, for aperture diameters of around 200 m.

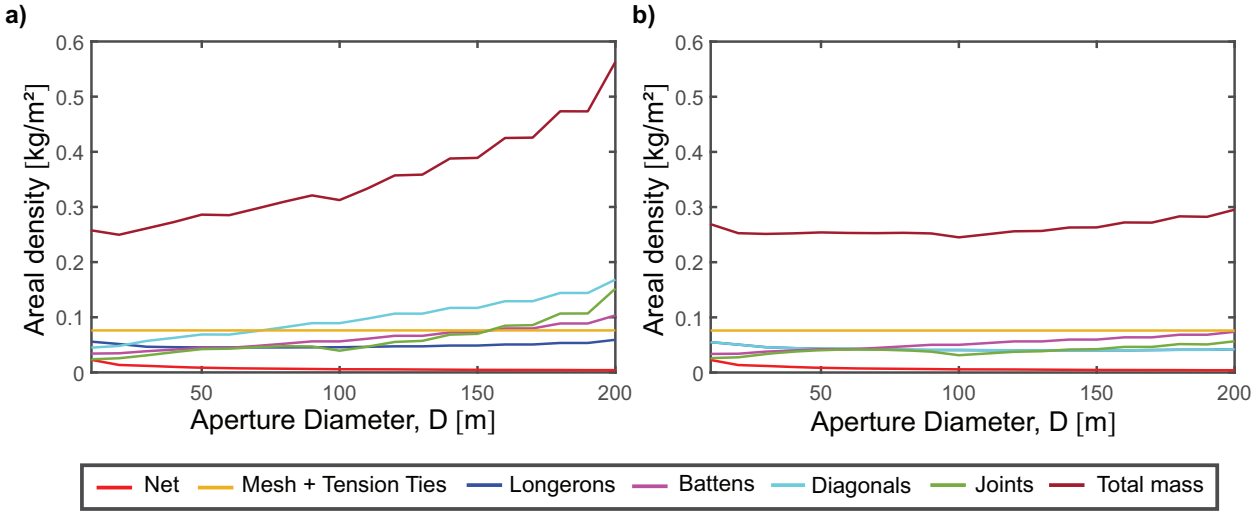

Fig. 4 Areal density of the reflector components ($F/D = 1.0$): a) non-optimal design, and b) optimal design

Figure 5 provides the overall mass (a), stowed diameter D_{stowed} (b), and stowed height H_{stowed} (c) of the deployable mesh reflector for the diameter range of 10 m to 200 m (in black solid lines). The total mass and stowed volume of the mesh reflector were identified to scale exponentially with increasing diameter. Two launch vehicles, the Falcon Heavy [28], and the Starship [29] were selected to evaluate the launch availability for mesh reflectors with a large aperture, the blue and pink solid lines in Fig. 5b, and c representing the payload limits for Falcon Heavy, and Starship, respectively. While the designs for all apertures lie well below the maximum payload mass limit to geostationary transfer orbit (GTO) of 26, 700 kg, the achievable aperture size is restricted by the launch envelope constraints, specifically that of the stowed diameter. Reflectors are limited to an aperture diameter of 70 m if launched in the Falcon Heavy, and launch in the larger Starship is limited to 100 m aperture. This scaling study leads to a valuable insight into the launch feasibility of deployable mesh reflectors designed by the outlined procedure consisting of established practices; it is volume-restricted. This highlights the limitations of deployable designs in achieving extremely large scale space-borne reflector antennas, and indicates that innovative designs and structure-building strategies such as on-orbit assembly may need to be explored to overcome the volumetric payload restrictions imposed by launch vehicles.

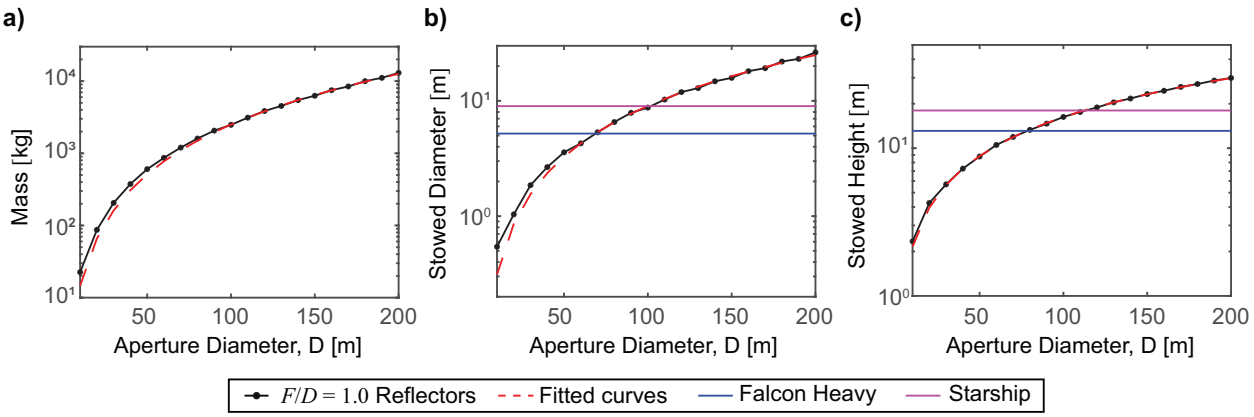

Fig. 5 Scaling of reflectors with $F/D = 1.0$: a) total mass, b) stowed diameter, and c) stowed height

B. Analytical scaling laws for mass and stowed volume

Based on the results of the scaling study outlined in Section III.A, the scaling laws for the mass and stowed envelope of the optimally designed deployable mesh reflector were established. As opposed to a simple approach where the total mass scales with D^2 (as per the overall areal density trend observed in Fig. 4b), a more detailed approach was followed to derive a mass scaling equation by grouping reflector components into three separate categories that scale in an equal manner based on the structural design process; the mass of the perimeter truss including the joints, the mass of the cable net, and the mass of the mesh and tension ties.

Each category of mass is expressed as a separate power function of D, as outlined in Fig. 6. The corresponding coefficients C_1, C_3 and C_5 are scaled to reflect the mass of deployment actuators, which remain at 10% of the total mass. The scaling law for reflectors with $F/D = 1.0$ is as follows;

$$M_{total} = 0.022D^{2.452} + 0.054D^{1.492} + 0.067D^2 \tag{11}$$

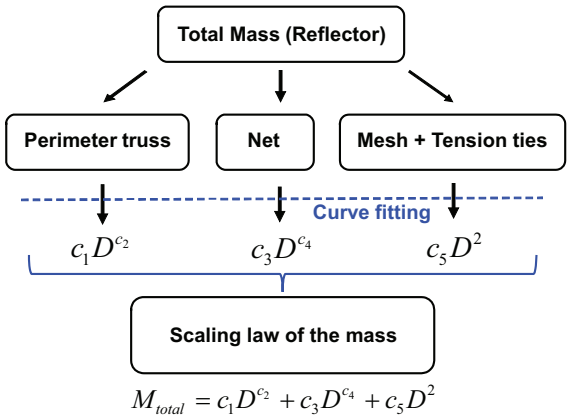

Fig. 6 Establishment of scaling law for the total mass

This analytical expression has been plotted (in red dashed lines) on Fig. 5a. It can be seen that these power functions of D very closely follow the trend of total mass of the reflector. There is negligible contribution of the cable nets, mesh and tensions ties to the stowed diameter and the height of the deployable reflector, as the size of stowed envelope is dominated by the perimeter truss members and the joints. Hence, single-term power functions were chosen to derive the analytical expressions for the scaling of the stowed diameter and height as indicated in the Eqs. (12) and (13), and plotted (in red dashed lines) on the Fig. 5b, and c.

$$D_{stowed} = 0.010D^{0.963} \tag{12}$$

$$H_{stowed} = 0.286D^{0.877} \tag{13}$$

IV. Scaling of Natural Frequencies of Vibration

A. Finite element model and boundary conditions

To investigate the scaling of natural frequency of the mesh reflector, a geometrically nonlinear finite element analysis was conducted using the commercial finite element package, Abaqus 2017. A high-fidelity finite element model was established, fully describing all structural elements. Cable nets were modeled as truss elements (T3D2), each edge of the triangulated facet consisting of a single truss element. Each strut in the perimeter truss was modeled with 20 beam elements (B31). The connections between two adjacent elements were pinned, which allows for relative rotational motion. The metallic mesh was modeled by equivalent point masses at each connecting node on the front net elements, the masses of joints and deployment actuators also modeled as point masses at the corresponding locations on the perimeter truss. A pre-defined stress field was applied to each structural component based on the prestress level obtained from the optimization process in Section II.B. Tension tie forces were applied to the inner nodes of the cable nets. Note that the numerical model is set up for the operational geometric configuration of the reflector under prestress, to avoid significant geometry changes when Abaqus computes the equilibrium geometry.

The natural frequency of the mesh reflector was evaluated for the range of diameters from 10 m to 200 m at intervals of 10 m. The boundary conditions were determined considering the practical configuration of operation, where the deployable mesh reflector is connected to the spacecraft via a supporting structure (*prime batten*), designed to secure the desired distance between the feed (most often installed on the spacecraft) and the reflector surface, and to allow for unimpeded perimeter truss deployment. As shown in Fig. 7a, the prime batten is connected to the perimeter truss via three joints in the upper rim of the truss, and one joint in the lower rim. This *batten-supported* boundary condition was realized in the finite element model by restricting 6 degrees-of-freedom (DoFs) of corresponding four joints in the perimeter truss as indicated in Fig. 7b.

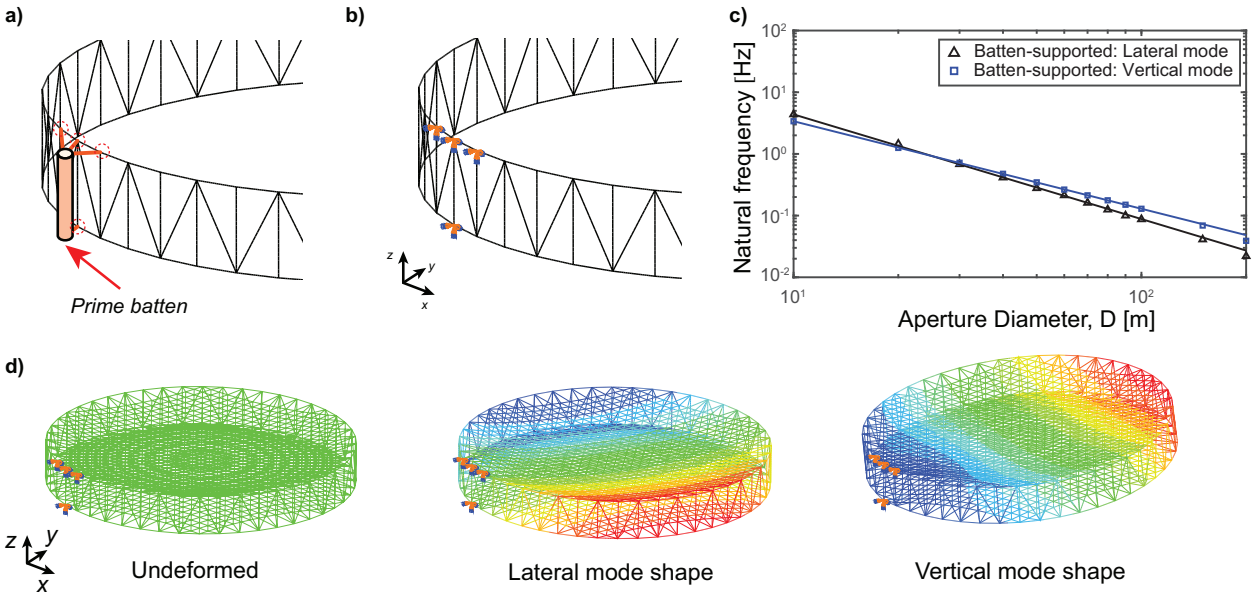

Fig. 7 Batten-supported boundary condition: a) illustration of the prime batten, and b) boundary condition in finite element model, Natural frequencies and mode shapes: c) natural frequency plots with fitted curves, and d) first two mode shapes for prime batten support

B. Analytical scaling law for the fundamental frequency and mode shapes

Figure 7c presents the natural frequencies of the mesh reflector for the batten-supported boundary condition, for $F/D = 1.0$. The study indicates that the lowest natural frequencies of the mesh reflector are proportional to a negative power function of the reflector diameter, as described by straight lines of negative slope in log-log space. For $D > 25$ m, the fundamental frequency corresponds to the lateral mode shape (see Fig. 7d), which indicates in-plane ($x - y$ plane in figure) vibrations as the structure rotates about the prime batten. As diameter decreases below 25 m, the modes swap,

the lateral mode becoming the second vibration mode, and the vertical mode (see Fig. 7d) becoming the fundamental mode. Here, the structure moves as a cantilever attached to the prime batten and vibrates mostly in the z direction.

The scaling law for the natural frequency with respect to the reflector diameter was established by fitting the modal analysis data to a power function of the diameter, as indicated in Fig. 7c. The results of high-fidelity simulations are represented by these fitted curves, with RMS error (RMSE) values of 0.014, and 0.003 Hz respectively for lateral and vertical mode frequencies. The corresponding analytical expressions for $F/D = 1.0$ are as follows;

$$f_{lateral} = 217.2 \times D^{-1.699} \tag{14}$$

$$f_{vertical} = 88.43 \times D^{-1.419} \tag{15}$$

C. Semi-analytical model for fundamental frequencies

While high-fidelity simulations provide accurate natural frequency and mode shape estimates for the reflector, the associated computational cost increases exponentially with increasing aperture size, and the number of structural elements. Hence, a scalable semi-analytical model for the mesh reflector, capable of estimating the natural frequency much faster, yet with fairly high accuracy was proposed.

The vibration modes obtained in Section IV.B was the basis of the semi-analytical model formulation. Figure 8 outlines the modeling scheme, based on homogenization of the mesh reflector structure. Here, the cable nets are modeled as a flat continuum disk with equivalent stiffness, with the perimeter truss homogenized to an equivalent hoop, attached to the perimeter of the disk to form an edge-stiffened disk.

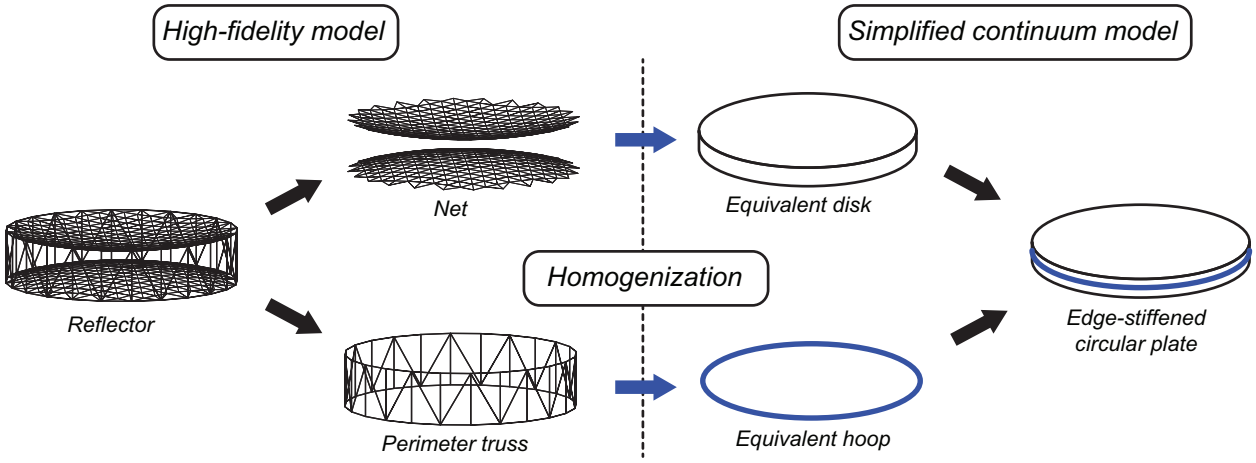

Fig. 8 Semi-analytical modeling scheme

The details of this scheme vary slightly, depending on the mode shape it is applied to. The scope of this study is limited to the derivation of the semi-analytical model for the lateral mode shape occurring for batten-supported boundary condition. Since the lateral mode shape is an in-plane vibration mode where the entire reflector rotates against the joints of the perimeter truss constrained by the prime batten (which can be assumed to be rigidly fixed), it can be represented by a single DoF mass-spring system as shown in Fig. 9a. The equivalent mass (M_{eq}) and moment of inertia (I_{eq}) are equal to the total mass and moment of inertia of the reflector for this case. The stiffness of the torsional spring (k_{eq}) attached to the rigid bar of length $D/2$ is obtained from the elastic analysis of an equivalent edge-stiffened continuum disk subject to the same boundary conditions as the reflector structure, and loaded by an external couple. Since the three fixed joints located in the upper layer of longerons has a higher contribution to the torsional stiffness corresponding to the lateral rotation of the structure (see Fig. 8), the semi-analytical model of the mesh reflector for the lateral mode only considers the front net and a single layer of longeron for the process of homogenization. Considering that the longerons are in perimeter of the front net, a circular hoop having the same cross-section as the longerons is attached to the perimeter of the homogenized disk, completing the semi-analytical model (i.e., edge-stiffened disk). The constraints applied by the prime batten on the edge of the front net is represented by the three supports of the disk. The homogenization process of the front net is summarized in the Fig. 9b, where the

cable elements are assumed to be coplanar (i.e., the curved shape of the net is neglected) and the net is assumed to be a uniform tessellation of equilateral triangles with edge length L.

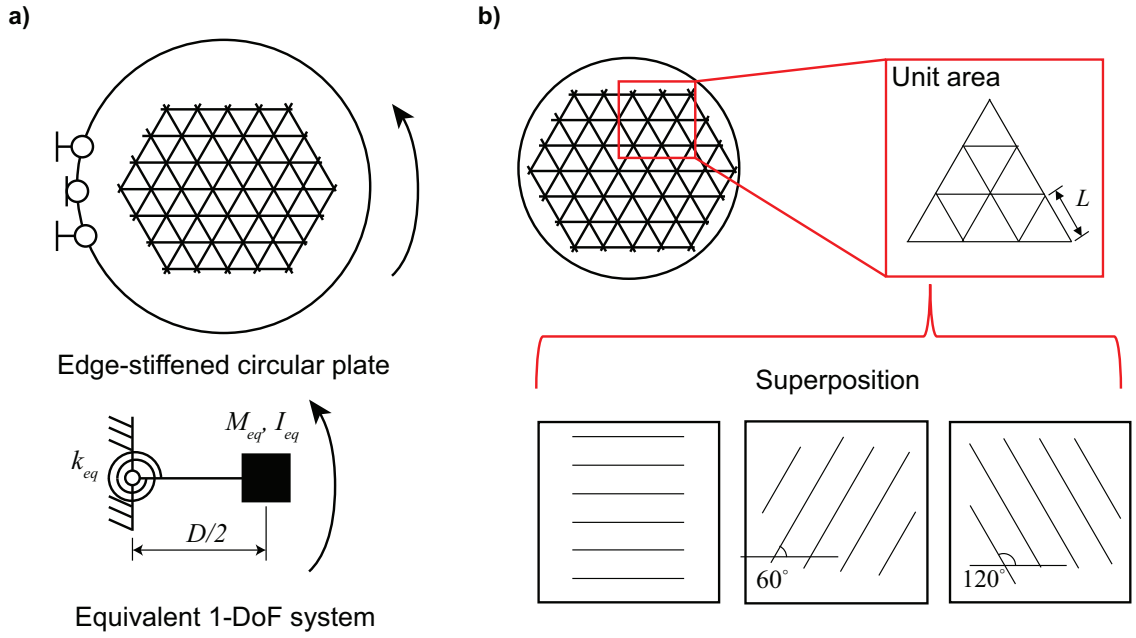

Fig. 9 Semi-analytical model to estimate lateral mode: a) 1-DoF model, and b) homogenization of the net

The homogenized stiffness matrix for a single-layer truss tessellation, A_{SL}, is calculated by superposition of three parallel truss tessellations [30], as shown in Fig. 9b.

$$A_{SL} = \frac{3\sqrt{3}E_w A_w}{4L} \tag{16}$$

where, E_w and A_w refer to the Young's modulus and the area of cross section of the truss respectively, and the equivalent continuum Young's modulus, E^*, and Poisson's ratio, ν^* of the equivalent disk model can be obtained from the typical constituent equations for a continuum of thickness t_w (Eqs. 17).

$$E^* = \frac{2\sqrt{3}E_w A_w}{3t_w L}, \quad \nu^* = \frac{1}{3} \tag{17}$$

The equivalent torsional stiffness of the 1-DoF system (k_{eq}) can be obtained by carrying out an elastic stiffness analysis of the edge-stiffened disk, measuring the rotation of the equivalent model under an applied moment. Combining these quantities, the natural frequency of the mesh reflector can be calculated from:

$$f_{lateral} = 2\pi\sqrt{\frac{k_{eq}}{M_{eq}D^2/4 + I_{eq}}} \tag{18}$$

Figure 10 compares the natural frequencies obtained from the finite element analysis with that obtained from the proposed semi-analytical approach. It can be seen that the results from the semi-analytical model are in good agreement with the results obtained from the prestressed modal analysis using the high-fidelity model. The results are also presented in Table 2, with the achievable levels of accuracy of the semi-analytical model in calculating the lateral mode frequency for the range of apertures of interest.

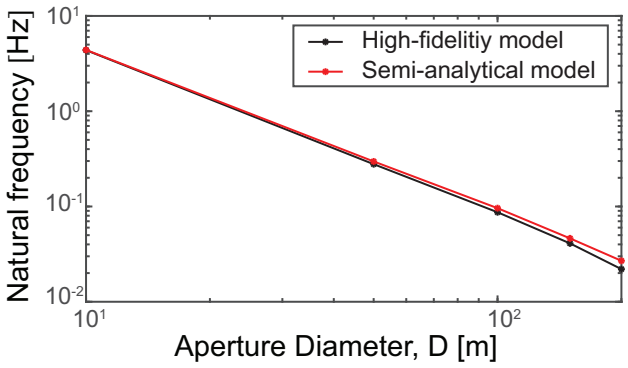

Fig. 10 Natural frequency corresponding to lateral mode

Table 2 Natural frequency: lateral model (high-fidelity model vs semi-analytical model)

	Natural frequency (Hz)		
D(m)	High-fidelity model	Semi-analytical model	Error (%)
10	4.346	4.371	0.58
50	0.276	0.294	6.54
100	0.086	0.095	10.30
150	0.041	0.046	12.39
200	0.022	0.027	22.27

V. Conclusion

This paper has presented a scalable design methodology for deployable mesh reflectors of 10−200 m size range. The surface of the reflector satisfies the surface accuracy requirement of 0.6 mm RMSE, enabling its use for a 10 GHz RF operational frequency. The study has focused on designs consisting of a complete triangular tessellation without any cross-wires to ensure both kinematic and statical determinacy of the structure and therefore achieve a unique shape and equilibrium solution under the prestressed state. The prestress distribution in the structure is optimized by varying the tension tie forces applied to the cable net, which led to a smaller standard deviation of prestress within the cable nets and lower compressive forces in the perimeter truss for the entire range of the apertures, compared to those of non-optimal designs. The structural design methodology has been established in detail, where member sizing is determined against critical structural failure criteria; minimum prestress level is determined in the cable net to prevent bowing during the operation and a safety factor of 2 is assumed against buckling failure. The mass of the reflector was investigated at the components level; the areal density of the optimized reflector stays almost constant with respect to the diameter, while the non-optimal design shows increasing areal density as the size of the reflector increases. The mass and stowed volume of the reflector are found to be exponentially proportional to the diameter of the reflector; the scaling laws of the mass and volume were derived as a function of the diameter. The scaling study on the mass, stowed diameter, and height of the structures indicate launch feasibility only up to around $D = 100$ m for commercially available launch vehicles, with a volume-constrained launch envelope, as opposed to mass-constrained. Volume constraints are inevitable in the design of deployable reflectors; thus, the results raise the need for novel construction methodologies for extremely large space-borne structures. The natural frequency of the reflector has been investigated for the batten-supported boundary condition, and scaling law of the fundamental frequency are then proposed based on the high-fidelity simulation results. For the purpose of estimating the natural frequency while reducing extreme computational costs associated with high-fidelity simulations for large reflectors, a semi-analytical model of the reflector has been proposed for the lateral mode shape of vibration for the batten-supported boundary condition. The semi-analytical model is based on the homogenization of the cable net and perimeter truss, with equivalent properties in the continuum. The estimated natural frequency from the semi-analytical model show good agreement with high-fidelity simulation results with the additional benefit of significantly reduced computational costs.

Acknowledgments

This research was funded by the DARPA NOM4D program, directed by Dr. Andrew Detor, under grant HR001122C0054.

References

[1] Roederer, A. G., and Rahmat-Samii, Y., "Unfurlable satellite antennas-a review," *Annales des télécommunications*, Vol. 44, 1989. https://doi.org/10.1007/BF02995012.

[2] Russell, R., Campbell, T., and Freeland, R., "A technology development program for large space antennas," Tech. rep., 1980.

[3] Miura, K., et al., "Research and development of the tension truss antenna," Tech. rep., IAF-87-317, 1987.

[4] Miura, K., and Miyazaki, Y., "Concept of the tension truss antenna," *AIAA Journal*, Vol. 28, No. 6, 1990, pp. 1098–1104. https://doi.org/10.2514/3.25172.

[5] Hedgepeth, J. M., "Influence of fabrication tolerances on the surface accuracy of largeantenna structures," *AIAA Journal*, Vol. 20, No. 5, 1982, pp. 680–686. https://doi.org/10.2514/3.7936.

[6] Thomson, M. W., "The Astromesh deployable reflector," *IEEE Antennas and Propagation Society International Symposium. 1999 Digest. Held in conjunction with: USNC/URSI National Radio Science Meeting (Cat. No. 99CH37010)*, Vol. 3, IEEE, 1999, pp. 1516–1519. https://doi.org/10.1109/APS.1999.838231.

[7] Thomson, M., "AstroMesh deployable reflectors for ku and ka band commercial satellites," *20th AIAA International Communication Satellite Systems Conference and Exhibit*, 2002, p. 2032. https://doi.org/10.2514/6.2002-2032.

[8] Smith, T., Lee, B., Semler, D., and Chae, D., "A large S-band antenna for a mobile satellite," *Space 2004 Conference and Exhibit*, 2004, p. 6120. https://doi.org/10.2514/6.2004-6120.

[9] Entekhabi, D., Njoku, E. G., O'Neill, P. E., Kellogg, K. H., Crow, W. T., Edelstein, W. N., Entin, J. K., Goodman, S. D., Jackson, T. J., Johnson, J., et al., "The soil moisture active passive (SMAP) mission," *Proceedings of the IEEE*, Vol. 98, No. 5, 2010, pp. 704–716. https://doi.org/10.1109/JPROC.2010.2043918.

[10] Scialino, L., Ihle, A., Migliorelli, M., Gatti, N., Datashvili, L., van 't Klooster, N., and Santiago-Prowald, J., "Large deployable reflectors for telecom and earth observation applications," *CEAS Space Journal*, Vol. 5, No. 3-4, 2013, pp. 125–146. https://doi.org/10.1007/s12567-013-0044-7.

[11] Datashvili, L., Endler, S., Wei, B., Baier, H., Langer, H., Friemel, M., Tsignadze, N., and Santiago-Prowald, J., "Study of mechanical architectures of large deployable space antenna apertures: from design to tests," *CEAS Space Journal*, Vol. 5, No. 3-4, 2013, pp. 169–184. https://doi.org/10.1007/s12567-013-0050-9.

[12] Dongwu, Y., Yiqun, Z., Guigeng, Y., and Jingli, D., "Least-squares minimization of boundary cable tension ratios for mesh reflectors," *AIAA Journal*, Vol. 56, No. 2, 2018, pp. 883–888. https://doi.org/10.2514/1.J056222.

[13] Zhang, S., Zhang, S., Zhang, Y., and Ye, J., "Force density sensitivity form-finding design method for cable-mesh reflector antennas considering interactive effects between cable network and supporting truss," *Engineering Structures*, Vol. 244, 2021, p. 112722. https://doi.org/10.1016/j.engstruct.2021.112722.

[14] Li, T., Jiang, J., Deng, H., Lin, Z., and Wang, Z., "Form-finding methods for deployable mesh reflector antennas," *Chinese Journal of Aeronautics*, Vol. 26, No. 5, 2013, pp. 1276–1282. https://doi.org/10.1016/j.cja.2013.04.062.

[15] Yang, D., Zhang, Y., Li, P., and Du, J., "Numerical form-finding method for large mesh reflectors with elastic rim trusses," *Acta Astronautica*, Vol. 147, 2018, pp. 241–250. https://doi.org/10.1016/j.actaastro.2018.04.007.

[16] Li, P., Liu, C., Tian, Q., Hu, H., and Song, Y., "Dynamics of a deployable mesh reflector of satellite antenna: form-finding and modal analysis," *Journal of Computational and Nonlinear Dynamics*, Vol. 11, No. 4, 2016. https://doi.org/10.1115/1.4033440.

[17] Li, P., Liu, C., Tian, Q., Hu, H., and Song, Y., "Dynamics of a deployable mesh reflector of satellite antenna: parallel computation and deployment simulation," *Journal of Computational and Nonlinear Dynamics*, Vol. 11, No. 6, 2016. https://doi.org/10.1115/1.4033657.

[18] Morterolle, S., Maurin, B., Dube, J.-F., Averseng, J., and Quirant, J., "Modal behavior of a new large reflector conceptual design," *Aerospace Science and Technology*, Vol. 42, 2015, pp. 74–79. https://doi.org/10.1016/j.ast.2015.01.002.

[19] Siriguleng, B., Zhang, W., Liu, T., and Liu, Y., "Vibration modal experiments and modal interactions of a large space deployable antenna with carbon fiber material and ring-truss structure," *Engineering Structures*, Vol. 207, 2020, p. 109932. https://doi.org/10.1016/j.engstruct.2019.109932.

[20] Kraus, J. D., and Marhefka, R., *Antennas for all applications*, McGraw-Hill, 2002.

[21] Stutzman, W., and Thiele, G., *Antenna Theory and Design*, 3rd ed., John Wiley Sons, 2012.

[22] Tan, L. T., and Pellegrino, S., "Thin-shell deployable reflectors with collapsible stiffeners Part 1: approach," *AIAA Journal*, Vol. 44, No. 11, 2006, pp. 2515–2523. https://doi.org/10.2514/1.16320.

[23] Agrawal, P., Anderson, M., and Card, M., "Preliminary design of large reflectors with flat facets," *IEEE Transactions on Antennas and Propagation*, Vol. 29, No. 4, 1981, pp. 688–694. https://doi.org/10.1109/TAP.1981.1142631.

[24] Calladine, C. R., "Buckminster Fuller's "tensegrity" structures and Clerk Maxwell's rules for the construction of stiff frames," *International Journal of Solids and Structures*, Vol. 14, No. 2, 1978, pp. 161–172. https://doi.org/10.1016/0020-7683(78)90052-5.

[25] Pellegrino, S., "Structural computations with the singular value decomposition of the equilibrium matrix," *International Journal of Solids and Structures*, Vol. 30, No. 21, 1993, pp. 3025–3035. https://doi.org/10.1016/0020-7683(93)90210-X.

[26] Tibert, A., and Pellegrino, S., "Deployable tensegrity reflectors for small satellites," *Journal of Spacecraft and Rockets*, Vol. 39, No. 5, 2002, pp. 701–709. https://doi.org/10.2514/2.3867.

[27] *M55J High modulus carbon fiber*, Toray Composite Materials America, Inc., January 2020. Rev. 2.0.

[28] *Falcon User's Guide*, SpaceX, September 2021.

[29] *Starship Users Guide*, SpaceX, March 2020.

[30] Miura, K., and Pellegrino, S., *Forms and concepts for lightweight structures*, Cambridge University Press, 2020. https://doi.org/10.1017/9781139048569.